Smart Structures and Systems, *Vol. 31, No. 6 (2023) 601-619*
https://doi.org/10.12989/sss.2023.31.6.601

Accuracy assessment of real-time hybrid testing for seismic control of an offshore wind turbine supporting structure with a TMD

Ging-Long Lin [1a], Lyan-Ywan Lu*[2], Kai-Ting Lei [2b], Shih-Wei Yeh [3c] and Kuang-Yen Liu [2d]

[1] *Department of Construction Engineering, National Kaohsiung University of Science and Technology, 1 University Road, Kaohsiung 824, Taiwan*
[2] *Department of Civil Engineering, National Cheng Kung University, 1 University Road, Tainan 701, Taiwan*
[3] *National Center for Research on Earthquake Engineering, Tainan, Taiwan*

(*Received May 8, 2022, Revised September 17, 2022, Accepted June 13, 2023*)

Abstract. In this study, the accuracy of a real-time hybrid test (RTHT) employed for a performance test of a tuned mass damper (TMD) on an offshore wind turbine (OWT) with a complicated jacket-type supporting structure is quantified and evaluated by comparing the RTHT results with the experimental data obtained from a shaking table test (STT), in which a 1/25-scale model for a typical 5-MW OWT controlled by a TMD was tested. In the RTHT, the jacket-type OWT structure was modelled using both multiple-DOF (MDOF) and single-DOF (SDOF) numerical models. When compared with the STT test data, the test results of the RTHT show that while the SDOF model, which requires less control computational time, is able to well predict the peak responses of the nacelle and TMD only, the MDOF model is able to effectively predict both the peak and over-all time-history responses at multiple critical locations of an OWT structure. This also indicates that, depending on the type of structural responses considered, an RTHT with either an SDOF or a MDOF model may be a promising alternative to the STT to assess the effectiveness of a TMD for seismic mitigation in an OWT context.

Keywords: jacket structure; offshore wind turbine; real-time hybrid test; seismic vibration control; shaking table test; system identification; tuned mass damper

1. Introduction

Evaluating the control effectiveness of a specific structural control device via a traditional earthquake engineering experimental method, such as shaking table test (STT), usually requires the construction of a test model incorporating the control device. The experiment becomes very costly when a large-scale test model is considered in the test. Therefore, most STTs must be modified to adapt to scaled-down tested models, which inevitably results in a scaling effect. To this end, a newly developed substructure testing technique called a hybrid test (HT) (Wu *et al*. 2007, Tu *et al*. 2010, Facchinetti and Bruni 2012, Tu 2013, Drazina and Govindjee 2017) has great advantages for testing structures incorporating full-scale control devices (McCrum and Williams 2016). In an HT, the controlled structural system to be investigated is divided into substructures. Only the substructure with the control device is physically tested, while the remaining substructures are numerically simulated. The simulated responses of the numerical substructures are obtained through an experimental apparatus, such as a hydraulic actuator, in order to interact with the physical substructure. The use of an HT technique significantly reduces the cost of the experiment. Recently, advances in sensing, actuation, and computation technologies have resulted in significant advancements in the HT technique.

The HT technique can be further classified into the following two categories: a pseudo-dynamic hybrid test (PDHT) and a real-time hybrid test (RTHT). The concept of the PDHT was first proposed by Hakuno *et al*. (1969). PDHT experiments are typically conducted at a slow rate and are generally applied to test nonlinear structural systems with displacement-dependent mechanical characteristics (Mahin and Shing 1985, Takanashi and Nakashima 1987, Khoo *et al*. 2016, Chang *et al*. 2017, Wang *et al*. 2019). This type of test usually places less demand on the hydraulic power and flow rate than other alternatives. On the other hand, RTHT experiments are typically conducted in real-time and are generally applied to test structural systems with velocity-dependent mechanical characteristics (Nakashima *et al*. 1992, Horiuchi *et al*. 1999, Shao *et al*. 2014, Chen *et al*. 2014, Asai *et al*. 2015, Chen *et al*. 2015, Chae *et al*. 2017). Time delay also becomes an issue when conducting a real-time test (Carrion and Spencer 2008, Wang *et al*. 2014, Hayati and Song 2017, Wang *et al*. 2020, Zhou and Li 2021). Iemura *et al*. (1999) further suggested incorporating a shaking table into the RTHT experiment, so the motion of the numerical substructures can be simulated by the shaking table, which usually leads

*Corresponding author, Professor,
E-mail: lylu@ncku.edu.tw
[a] Associate Professor
[b] Graduate Assistant
[c] Associate Technologist
[d] Associate Professor

ISSN: 1738-1584 (Print), 1738-1991 (Online)

to higher control accuracy. This testing technique, also called a real-time hybrid shaking table test (RTHSTT), has great potential for application in the field of earthquake engineering research and deserves further development and verification (Igarashi et al. 2000, Reinhorn *et al*. 2003, Neild *et al*. 2005, He and Jiang 2019, Chen *et al*. 2019, Lu *et al*. 2019).

Offshore wind turbines (OWTs) are often erected to generate clean renewable energy. In the case of OWTs located in seismically active areas, structural control technologies may be adopted to protect the OWTs from supporting-structure damage or nacelle equipment breakdowns under seismic attacks. A tuned mass damper (TMD) can be an effective control device used to mitigate seismic responses in an OWT structure since TMDs have been proven to be promising protective devices for slender structures, such as high-rise buildings, as discussed in the literature (Lin *et al*. 1994, 1999, Connor 2002, Yang *et al*. 2021). TMD-type devices used for vibration mitigation of wind turbines under wind, wave, earthquake, and blade-tower interaction loadings have also been investigated by many researchers. The TMDs in these studies had various forms, such as mass dampers with a solid mass block (Lackner and Rotea 2011, Zhao *et al*. 2018, Jin *et al*. 2018, Ju and Huang 2019, Lin *et al*. 2021), tuned liquid column dampers (TLCDs) (Colwell and Basu 2009, Bargi *et al*. 2016), ball vibration absorbers (Chen and Georgakis 2013, Li *et al*. 2012, Zhang *et al*. 2014), etc. Experimental verification on the effectiveness of these types of TMDs is generally required.

In order to reduce experimental costs, the aforementioned RTHT technique has been employed by researchers to experimentally evaluate the control performance of TMD-type devices used in slender or flexible structures. In 2000, Igarashi *et al*. (2000) and Horiuchi *et al*. (2000) were among the first authors to propose the RTHT methodology using a shaking table to simulate the motion of a primary system interacting with an attached secondary system (physical substructure). Igarashi *et al*. (2004) also conducted an RTHT to mimic the interaction behavior between a nonlinear bridge column (numerical substructure) and a TMD (physical substructure). Lee *et al*. (2007) conducted an RTHT to evaluate the dynamic responses of a three-story building controlled by a tuned liquid damper (TLD) under earthquake conditions. Zhu *et al*. (2017) employed an RTHT with a shaking table to verify full-scale TLCDs and demonstrated the interaction of a nine-story building with multiple TLCDs. The soil-structure interaction (SSI) was also considered in their study. Chu *et al*. (2018) and Yeh (2017) applied an RTHT to test the feasibility of controlling a single degree-of-freedom (SDOF) primary structure by using a mass damper with a semi-active friction device (Lu *et al*. 2011). In their tests, the reliability of the RTHT results was verified by using the experimental results for an STT. Fu *et al*. (2019) conducted an RTHT to evaluate the seismic control performance of particle dampers installed on a single-story steel frame (numerical substructure). Chen *et al*. (2020) examined the control effectiveness of a building mass damper (BMD) for seismic vibration reduction via an RTHT. Additionally, compensation techniques were applied to the RTHT to improve the test accuracy. Zhang *et al*. (2016) and Zhang *et al*. (2019) conducted an RTHT with full-scale TLDs as the physical substructures, and a multiple-DOF wind turbine model was used as the numerical substructure. The interaction force between the TLDs and the wind turbine exerted by wind-wave loading was simulated physically using hydraulic actuators in the RTHT.

The results obtained in all the above references showed that the RTHT technique can be a cost effective means by which to physically evaluate the control efficiency of TMD-type devices. Nevertheless, like other new testing methods, the accuracy of RTHT results should be verified and calibrated through other reliable experimental means during its developmental stage. The verification of most of the RTHTs conducted in previous studies was only carried out through a pure numerical simulation of the complete model, rather than through another independent experimental approach, such as an STT; therefore, the reliability and accuracy of the RTHT results could not be evaluated or verified. Furthermore, in order to reduce on-line control computational time, most of the previous TMD-RTHT studies adopted a simplified SDOF model rather than a more accurate model with multiple DOFs for the numerical substructures. The SDOF model may inevitably induce larger modeling error in the RTHT, and more importantly, it cannot provide sufficient test results if the dynamic responses at multiple locations on the structure are of interest. Therefore, it is desirable to acquire more RTHT testing evidence for numerical substructures with multiple DOFs (Calabrese *et al*. 2015).

By directly using STT test data with a complete model to reflect the accurate result, the objective of this study is to quantify and compare the accuracy of the RTHT employed for a performance test of a TMD installed on an OWT structure when the structure is modelled using an SDOF and multiple-DOF (MDOF) models, respectively. The prototype OWT considered in the study is a 5 mega-watt (5MW) OWT with a complicated jacket-type supporting structure. This type of OWT is particularly suitable for a deep-water wind farm and is very commonly used for the OWTs built in the Taiwan Strait area due to the properties of the seabed and the natural environmental challenges (such as earthquakes and typhoons) (Ju *et al*. 2019a, b). Based on the specifications for a 5-MW jacket-type OWT as suggested by the National Renewable Energy Research Center (NREL, USA) (Jonkman *et al*. 2009), in this study, a 1/25 scaled-down tested model and its corresponding TMD were fabricated for both the STT and the RTHT, and their results were compared. Moreover, in the RTHT, in order to obtain a reduced-order MDOF model for the numerical substructure, a general system identification procedure using subspace identification (SID) technique is proposed in this study. In this procedure, the state-space matrices representing the reduced-order model can be identified experimentally by using the measured responses of an existing structure (or prototype), or numerically by using the simulated responses of a pre-established finite-element structural model.

The paper is organized as follows: In Section 2, based on the state-space formulation, the dynamic equations and transfer function matrix for the OWT numerical model used in the RTHT are derived, and the invariance of the transfer function matrix under a coordinate transformation is proven. Section 3 discusses the STT conducted for the complete 1/25-scale jacket-type OWT-TMD model (hereafter called the complete STT), and the investigation of the effectiveness of the use of a TMD for OWT seismic mitigation is discussed. In Section 4, by using the SID technique, the state-space matrices for the MDOF OWT numerical model used in the RTHT are identified experimentally. Section 5 discusses the RTHTs conducted for the OWT-TMD system, and the test results are compared with those of the complete STT under the same seismic excitations, so the advantages and accuracy of the RTHT using the SDOF and MDOF OWT structural models can be evaluated, compared, and discussed. Finally, the conclusion is given in Section 6.

2. RTHT for OWT-TMD system with a jacket-type supporting structure

2.1 Substructuring of the OWT-TMD system

Fig. 1(a) shows the complete model of the OWT-TMD system with a jacket-type supporting structure and a pile foundation considered in this study. For simplicity, in this model, the nacelle of the OWT is represented by a mass block without considering the dynamic effect of the rotating blades. For the purposes of the RTHT, as shown in Fig. 1(b), the model is further divided into two substructures: the TMD (the physical substructure) and the OWT with the jacket structure and piles (the numerical substructure). In the RTHT, the TMD was physically tested, while the responses of the OWT structure were numerically simulated. The OWT numerical substructure was subjected to two input excitations: ground acceleration $\ddot{x}_g(t)$ and the TMD-force $s(t)$, which is an interaction force between the numerical OWT model and the physical TMD specimen. In order to establish the numerical model to be used in the RTHT, it was necessary to derive the equation of motion for the OWT substructure.

2.2 Dynamic equation for the OWT substructure

Based on the numerical substructure shown in Fig. 1(b), the equation of motion for the OWT structure can be written as

$$\mathbf{M}\ddot{\mathbf{x}}(t)+\mathbf{C}\dot{\mathbf{x}}(t)+\mathbf{K}\mathbf{x}(t)=-\mathbf{M}\mathbf{L}_g\ddot{x}_g(t)+\mathbf{L}_s\, s(t) \tag{1}$$

$$\mathbf{x}(t)=[x_{jb}(t)\quad x_{tb}(t)\quad x_n(t)]^T \tag{2}$$

where $\mathbf{M}$, $\mathbf{C}$, and $\mathbf{K}$ denote the mass, damping, and stiffness matrices of the OWT structure, respectively, and $\ddot{x}_g(t)$ is the ground acceleration. The vectors $\boldsymbol{x}$, $\dot{\boldsymbol{x}}$, and $\ddot{\boldsymbol{x}}$ represent the relative-to-the-ground displacement, velocity, and acceleration vectors of the OWT structure, respectively. The vectors $\mathbf{L}_g$ and $\mathbf{L}_s$ represent the placement vectors for $\ddot{x}_g(t)$ and $s(t)$, respectively. In Eq. (2), the symbols x_{jb}, x_{tb}, and x_n represent the relative displacements measured at the jacket base, tower base, and nacelle, respectively (see Fig. 1(b)). Eqs. (1) and (2) indicate that the OWT structure is modelled as a 3-DOF system in this study, where the three DOFs of interest are the responses at the jacket base, tower base, and nacelle since the responses of these locations are most representative and have significant relevance in the field of engineering. Furthermore, in Eq. (1), the interaction force $s(t)$ exerted by the TMD can be written as (see Fig. 1(b)).

$$s(t)=-m_d\, a_d(t) \tag{3}$$

where m_d and $a_d(t)$ are the mass and the absolute acceleration of the TMD measured in the test, respectively. In addition, the damping coefficient and spring stiffness of the TMD are represented by the symbols c_d and k_d in Fig. 1(b), respectively.

Furthermore, because in the RTHT, the nacelle's absolute acceleration, as simulated by the numerical model, is taken as the input excitation for the tested physical substructure (the TMD). Let us define a system output vector $\mathbf{y}$, i.e.

$$\mathbf{y}(t)=[a_{jb}(t)\quad a_{tb}(t)\quad a_n(t)]^T \tag{4}$$

where a_{jb}, a_{tb}, and a_n represent the absolute accelerations of the jacket base, tower base, and nacelle, respectively. Using the definitions from Eqs. (1) and (4), the relationship between the absolute accelerations $\mathbf{y}$ and the relative accelerations $\ddot{\boldsymbol{x}}$ can be written as

$$\mathbf{y}(t)=\ddot{\mathbf{x}}(t)+\mathbf{L}_g\,\ddot{x}_g(t) \tag{5}$$

In order to facilitate real-time on-line computation of the numerical model, Eqs. (1) and (5) are further expressed in a standard state-space form as follows

$$\dot{\mathbf{z}}(t)=\mathbf{A}\,\mathbf{z}(t)+\mathbf{B}\,\mathbf{u}(t) \tag{6}$$

$$\mathbf{y}(t)=\mathbf{C}\,\mathbf{z}(t)+\mathbf{D}\,\mathbf{u}(t) \tag{7}$$

where $\mathbf{z}$ denotes the state vector; $\mathbf{u}$ is the input vector (the excitation vector); $\mathbf{y}$ is the output vector; $\mathbf{A}$ is the system matrix; $\mathbf{B}$ is the input influence matrix; $\mathbf{C}$ is output influence matrix, and $\mathbf{D}$ is the feedforward matrix. The content of these vectors and matrices are listed below.

$$\mathbf{z}(t)=\begin{Bmatrix}\dot{\mathbf{x}}(t)\\ \mathbf{x}(t)\end{Bmatrix},\qquad \mathbf{u}(t)=\begin{Bmatrix}\ddot{x}_g(t)\\ s(t)\end{Bmatrix} \tag{8a}$$

$$\mathbf{A}=\begin{bmatrix}-\mathbf{M}^{-1}\mathbf{C} & -\mathbf{M}^{-1}\mathbf{K}\\ \mathbf{I} & \mathbf{0}\end{bmatrix},\qquad \mathbf{B}=\begin{bmatrix}-\mathbf{L}_g & \mathbf{M}^{-1}\mathbf{L}_s\\ \mathbf{0} & \mathbf{0}\end{bmatrix} \tag{8b}$$

$$\mathbf{C}=\begin{bmatrix}-\mathbf{M}^{-1}\mathbf{C} & -\mathbf{M}^{-1}\mathbf{K}\end{bmatrix},\qquad \mathbf{D}=\begin{bmatrix}\mathbf{0} & \mathbf{M}^{-1}\mathbf{L}_s\end{bmatrix} \tag{8c}$$

Notably, Eq. (7) is obtained by substituting Eq. (1) into Eq. (5). In the RTHT in this study, the OWT numerical model was established based on the state-space matrices shown in Eqs. (8b) and (8c) (i.e., the $\mathbf{A}$, $\mathbf{B}$, $\mathbf{C}$, and $\mathbf{D}$ matrices), whose numerical values were identified in the complete STT to be discussed in Section 3.

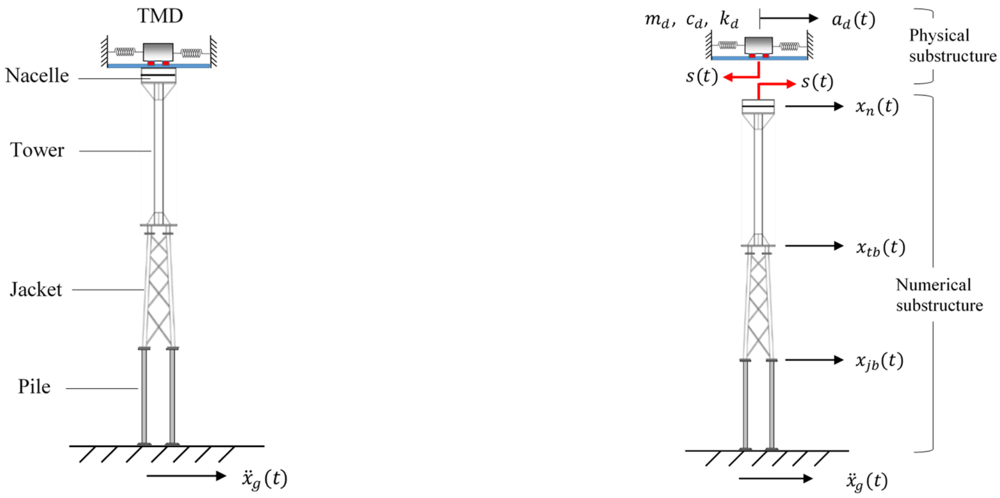

(a) Complete model (b) Substructuring for the RTHT

Fig. 1 The tested OWT model with a jacket-type supporting structure controlled using a TMD

2.3 Transfer function matrix of the OWT substructure

The dynamic property of the OWT substructure system described by the state-space equations, Eqs. (6) and (7), may also be characterized by its transfer functions, which define the relationship between the system inputs and outputs. To obtain the transfer functions, one may take the Fourier transform on both sides of Eqs. (6) and (7). Combining the Fourier transform results from Eqs. (6) and (7) yields the following relationship between the system inputs and outputs in the (ω) frequency domain (Ljung 1999)

$$\mathbf{Y}(\omega) = \mathbf{G}(\omega)\,\mathbf{U}(\omega) \tag{9}$$

where $\mathbf{U}(\omega)$ and $\mathbf{Y}(\omega)$ are the Fourier transforms of the input vector $\mathbf{u}$ and output vector $\mathbf{y}$, respectively, and $\mathbf{G}(\omega)$ is the transfer function matrix that can be expressed as

$$\mathbf{G}(\omega) = \mathbf{C}(i\omega\mathbf{I} - \mathbf{A})^{-1}\mathbf{B} + \mathbf{D} \tag{10}$$

Notably, $\mathbf{G}(\omega)$ is a complex matrix, even though the state-space matrices ($\mathbf{A}$, $\mathbf{B}$, $\mathbf{C}$, $\mathbf{D}$), defined in Eqs. (8b) and (8c), are real-number matrices.

2.4 Invariance of transfer function matrix

In general, the seismic response of an OWT structure can be more accurately simulated using a finite-element numerical model with a large number of DOFs. However, to perform the RTHT in real-time, the order of the numerical model has to be reduced. Furthermore, due to the complexity of an OWT with a jacket-type supporting structure, it is a challenging task to construct a set of precise structural matrices (i.e., the $\mathbf{M}$, $\mathbf{C}$ and $\mathbf{K}$ matrices in Eq. (1)) with only a few DOFs. Therefore, to overcome this challenge, in this study, the state-space matrices (i.e., $\mathbf{A}$, $\mathbf{B}$, $\mathbf{C}$, and $\mathbf{D}$ in Eqs. (6) and (7)) for the numerical OWT structure with only three DOFs (i.e., x_{jb}, x_{tb}, and x_n in Eq. (2)) were directly acquired from a system identification test conducted on the 1/25-scale OWT model prior to the RTHT. Then, the identified state-space matrices were used in the RTHT. However, for a given linear system, the state-space matrices identified from a system identification test may not be unique due to the state-vector coordinate transformation, so they may not be the same as those determined using Eqs. (8b) and (8c). On the other hand, it will be proven in this section that the transfer function matrix $\boldsymbol{G}(\omega)$ computed using Eq. (10) will remain unchanged under the coordinate transformation of the state vector. This feature, the invariance of transfer function matrix, will be employed to verify the suitability of the identified state-space matrices.

To prove that the transfer function matrix is invariant, let $\boldsymbol{z}(t)$ and $\bar{\boldsymbol{z}}(t)$ represent the state vectors observed in the original and new coordinate systems, respectively, which are related by

$$\mathbf{z}(t) = \mathbf{T}\,\bar{\mathbf{z}}(t), \quad \dot{\mathbf{z}}(t) = \mathbf{T}\,\dot{\bar{\mathbf{z}}}(t) \tag{11}$$

where $\mathbf{T}$ denotes the coordinate transformation matrix. Using Eq. (11) in Eqs. (6) and (7) yields a set of new state-space equations

$$\dot{\bar{\mathbf{z}}}(t) = \overline{\mathbf{A}}\,\bar{\mathbf{z}}(t) + \overline{\mathbf{B}}\,\mathbf{u}(t) \tag{12}$$

$$\mathbf{y}(t) = \overline{\mathbf{C}}\,\bar{\mathbf{z}}(t) + \overline{\mathbf{D}}\,\mathbf{u}(t) \tag{13}$$

where $\bar{\boldsymbol{A}}$, $\bar{\boldsymbol{B}}$, $\bar{\boldsymbol{C}}$, and $\bar{\boldsymbol{D}}$ represent the state-space matrices in the new coordinate system, which can be expressed as

$$\overline{\mathbf{A}} = \mathbf{T}^{-1}\mathbf{A}\mathbf{T}, \; \overline{\mathbf{B}} = \mathbf{T}^{-1}\mathbf{B}, \; \overline{\mathbf{C}} = \mathbf{C}\mathbf{T}, \; \overline{\mathbf{D}} = \mathbf{D} \tag{14}$$

Eq. (14) also describes the relationship of the state-space matrices in the two different coordinate systems. Using Eq. (10), the transfer function matrix $\bar{\boldsymbol{G}}(\omega)$ in the new coordinate system can be written as

$$\overline{\mathbf{G}}(\omega) = \overline{\mathbf{C}}(i\omega\mathbf{I} - \overline{\mathbf{A}})^{-1}\overline{\mathbf{B}} + \overline{\mathbf{D}} \tag{15}$$

Next, using Eq. (14) in Eq. (15) and letting

$$\mathbf{I} = \mathbf{T}^{-1}\,\mathbf{I}\,\mathbf{T} \tag{16}$$

leads to

$$\begin{aligned}\overline{\mathbf{G}}(\omega) &= \mathbf{C}\,\mathbf{T}\left[\mathbf{T}^{-1}(i\omega\mathbf{I}-\mathbf{A})\,\mathbf{T}\right]^{-1}\mathbf{T}^{-1}\,\mathbf{B}+\mathbf{D}\\ &= \mathbf{C}\,\mathbf{T}\left[\mathbf{T}^{-1}(i\omega\mathbf{I}-\mathbf{A})^{-1}\mathbf{T}\right]\mathbf{T}^{-1}\,\mathbf{B}+\mathbf{D}\\ &= \mathbf{C}\,(i\omega\mathbf{I}-\mathbf{A})^{-1}\mathbf{B}+\mathbf{D}\\ &= \mathbf{G}(\omega)\end{aligned} \tag{17}$$

Eq. (17) states that the transfer function matrix $\boldsymbol{G}(\omega)$ remains unchanged under a coordinate transformation. The above discussion also indicates that for a given linear system, there exists only one transfer function matrix $\boldsymbol{G}(\omega)$ even though there are infinite possible sets of space-space matrices. This is a great advantage for performing the RTHT discussed in a later section. Because of transfer function matrix invariance, any set of state-space matrices ($\bar{\boldsymbol{A}}$, $\bar{\boldsymbol{B}}$, $\bar{\boldsymbol{C}}$, and $\bar{\boldsymbol{D}}$) identified through a dynamic test in the time domain can be employed to numerically represent the physical OWT structure, as long as one can prove that the transfer function matrix $\boldsymbol{G}(\omega)$ computed based on these identified state-space matrices (through Eq. (10)) is consistent with the one obtained directly from a modal test in the frequency domain. In the later RTHT, these identified $\bar{\boldsymbol{A}}$, $\bar{\boldsymbol{B}}$, $\bar{\boldsymbol{C}}$, and $\bar{\boldsymbol{D}}$ matrices will be used to represent the numerical OWT substructure.

3. Shaking table test with the complete OWT-TMD model

3.1 Test setup

In order to assess the accuracy of the RTHT, a shaking table test (STT) was conducted on a 1/25-scale OWT model with a scaled-down TMD. Since in this test, the complete OWT-TMD tested model without substructuring was used, the test is referred to hereafter as the 'complete STT.' The test was carried out using the 8×8 m shaking table in the Tainan Laboratory at the National Center for Research on Earthquake Engineering (NCREE, Taiwan). Fig. 2(a) shows a photo of the test setup in the complete STT. The corresponding scaled-down TMD was installed on the top of the OWT (i.e., on the nacelle). The weight of the nacelle, which constitutes a large portion of the total weight of the OWT model, was simulated with a mass block. Fig. 2(b) illustrates the sensor deployment in the STT. Optical sensors, called Motion Capture (MoCap), were used in the test to measure the absolute displacements of the model. As shown in Fig. 2(b), the time-history responses of the five spots on the scaled-down model, the TMD, the nacelle, the tower base, the jacket base, and the shaking table, were measured using accelerometers or the MoCap sensors.

The design of the 1/25-scale OWT tested model followed the specifications of a typical 5-MW OWT with the jacket structure suggested by Jonkman *et al*. (2009). To comply with the similarity law, the physical quantities of the model were designed such that the following rules were satisfied

$$\text{Length}_{\text{fullscale}} = \lambda\,\text{Length}_{\text{model}} \tag{18}$$

$$\text{Frequency}_{\text{full scale}} = \frac{1}{\sqrt{\lambda}}\,\text{Frequency}_{\text{model}} \tag{19}$$

$$\text{Acceleration}_{\text{full scale}} = \text{Acceleration}_{\text{model}} \tag{20}$$

In the above equations, the subscripts "full scale" and "model" denote that the quantities are associated with the full-scale system and the scaled-down model, respectively. The symbol λ represents the scale factor, which is equal to 25 in this study. According to Eq. (19), the natural frequency of the tested OWT model is ideally five times that of the full-scale structure, while Eq. (20) states that the accelerations for both systems are equal.

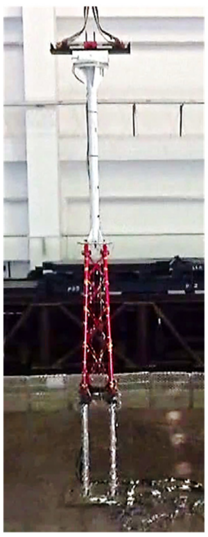

(a) Photo of the test setup

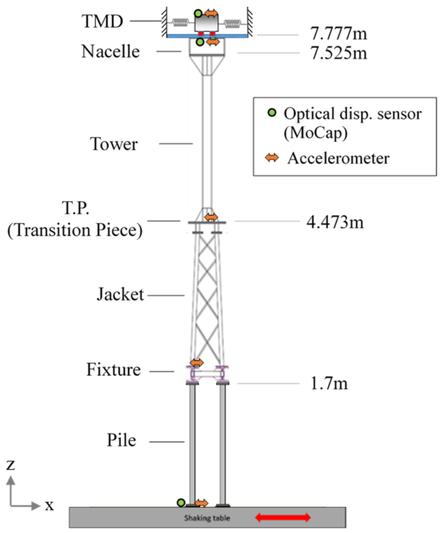

(b) Sensor deployment

Fig. 2 Setup for the shaking table test with the OWT-TMD testing model

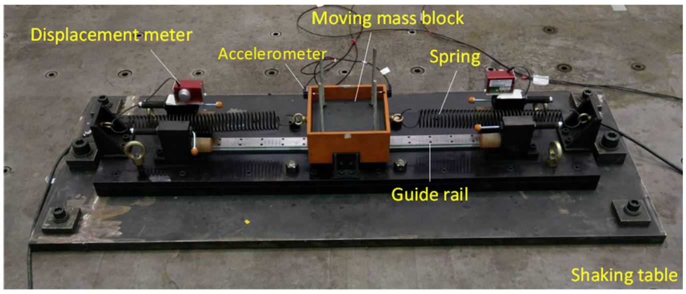

Fig. 3 Photo of the TMD and RTHT setup

Table 1 Parameters of the tested OWT when modelled as an SDOF structure

Parameter	Value
Mass (m_w)	1013 kg
Frequency (f_w)	1.09 Hz
Damping ratio (ξ_w)	0.15%

Table 2 Parameters of the tested TMD

Parameter	Value
Mass (m_d)	26.15 kg
Spring stiffness (k_d)	1142 N/m
Frequency (f_d)	1.05 Hz
Maximum stroke	± 0.3 m

An image of the TMD used in the test is shown in Fig. 3. The TMD was composed of a moving mass box, a linear guide rail, and two tensional springs that offer a restoring force to the TMD. The moving mass of the TMD could be changed by using mass blocks of different weights, so the TMD frequency could be adjusted by varying the number of mass blocks.

3.2 Design of TMD parameters

In the test, the optimal design formulas proposed by Lin *et al.* (1994) were adopted to determine the TMD parameters. The design optimization rule is aimed toward minimizing the mean-square response of the 1st modal displacement of the OWT under a white-noise ground excitation. Let μ and r_f represent TMD's mass ratio and frequency ratio, which can be written as

$$\mu = \frac{m_d}{m_w}, \qquad r_f = \frac{f_d}{f_w} \tag{21}$$

Where m_d and m_w represent the masses of the TMD and the OWT structure, respectively; f_d represents the TMD frequency, and f_w is the fundamental frequency of the OWT structure. Based on the formulas by Lin *et al.* (1994), the optimal frequency ratio $r_{f,opt}$ and damping ratio $\zeta_{d,opt}$ can be expressed as follows

$$r_{f,opt} = \left(\frac{a}{1+\mu}\right)^b, \qquad a = 1 - \frac{\zeta_w}{4}, \qquad b = 1.35e^{3.2\zeta_w} \tag{22}$$

$$\zeta_{d,opt} = 0.46\mu^{0.48} \tag{23}$$

where ζ_w is the damping ratio of the OWT structure.

In order to determine the parameters of the TMD, Table 1 lists the parameters of the 1/25-scale OWT structure, which when simplified, is an SDOF model. The total mass of the OWT tested model was 1013kg. The identified 1st modal frequency and damping ratio were 1.09 Hz and 0.15%, respectively. These values were obtained from the Fourier spectrum of the nacelle's acceleration under a white noise ground acceleration, as shown in Fig. 4. Based on the OWT parameters given in Table 1 and the TMD design formulas given in Eqs. (22) and (23), Table 2 lists the parameters designed for the TMD used in the test. As

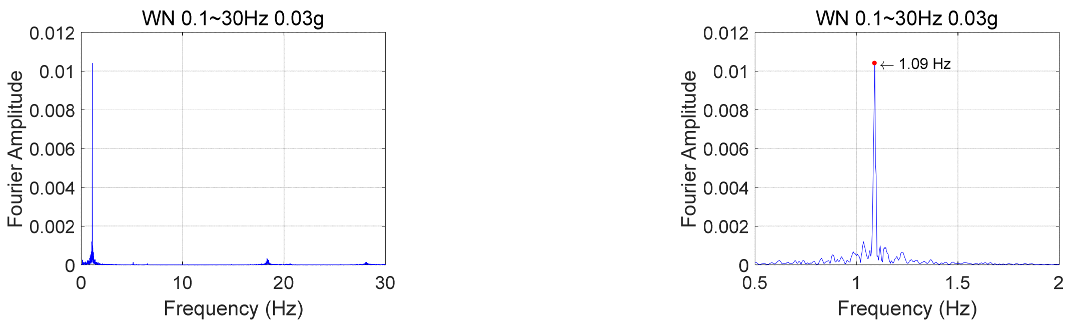

(a) Freq. range 0-30 Hz (b) Freq. range 0.5-2.0 Hz

Fig. 4 Fourier spectrum of the nacelle's acceleration under white noise ground acceleration (0-30 Hz, 0.03 g)

Table 3 Ground motions for the shaking table test and the RTHT

Earthquake	Station	Direction	Year	Original PGA	PGA used in test
Chi-Chi	TCU078	EW	1999	0.44 g	0.20 g, 0.25 g
Hua-Lien	HWA062	EW	2018	0.21 g	0.15 g, 0.20 g
Chi-Chi	TCU075	EW	1999	0.26 g	0.15 g, 0.20 g
Chi-Chi	TCU102	EW	1999	0.17 g	0.15 g, 0.20 g
Chi-Chi	TCU102	NS	1999	0.30 g	0.10 g

*Note: The durations of these ground accelerations were scaled to 1/5 that of the originals, in accordance with the similarity law

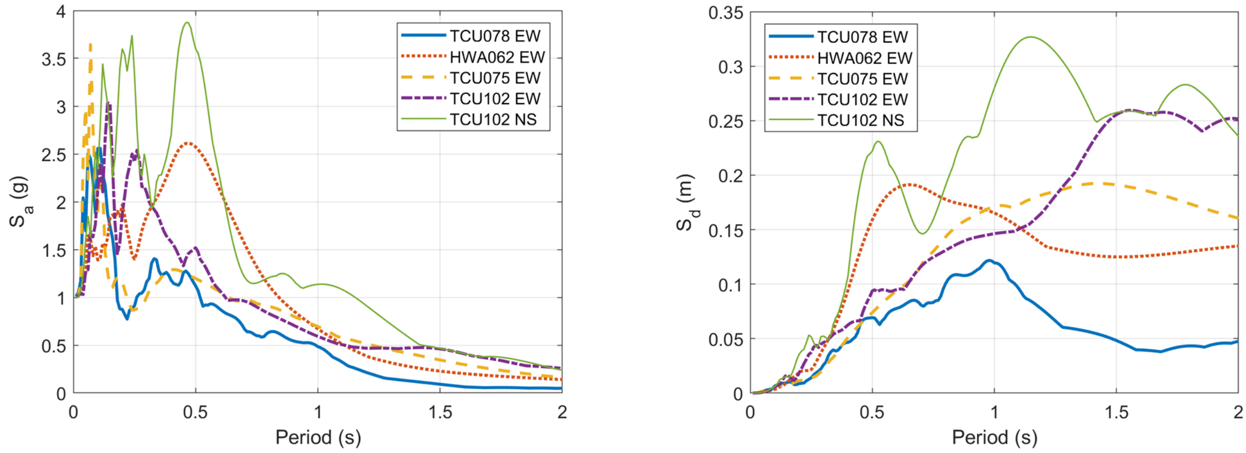

(a) Acceleration (b) Displacement

Fig. 5 Response spectra of ground motions (PGA scaled to 1.0 g, 5% damping ratio)

shown in Tables 1 and 2, the mass ratio μ of the TMD was equal to 2.58% (= 26.15/1013), which led to an optimal frequency ratio $r_{f,opt}$ of 0.96, and an optimal damping ratio $\zeta_{d,opt}$ of 8%, which was roughly achieved based on the TMD's sliding friction force.

3.3 Ground excitations

Two types of ground excitations were applied in the test: (1) a sine-sweep excitation and (2) an earthquake excitation. The duration of the sine sweep excitation was 120 seconds, with different peak ground acceleration (PGA) levels. The frequency of the sine sweep excitation increased from 0.1 to 2.0 Hz during the first half of the test period, and then decreased from 2.0 to 0.1 Hz during the second half. Five earthquake records listed in Table 3 were considered in the STT for the earthquake excitations. Among them, the Chi-Chi (TCU078) earthquake was an artificially modified ground motion, which was generated based on the actual time-history record taking into consideration the site characteristics of a wind-farm located off-shore of Chang-Hua, Taiwan. The Hua-Lien (HWA062) ground motion, recorded in the 2018 Hua-Lien earthquake, had near-fault earthquake characteristics with a pulse-like waveform. The other three earthquake records were also historical records measured during the Chi-Chi earthquake (1999) at different stations. According to the similarity rule given in Eq. (19), the time scaling factor had to be (1/5), so the durations of all ground motions were compressed into one-fifth of the original figures in the test. Fig. 5 shows the acceleration and displacement response spectra of these five ground motions used in the test, while their time histories are illustrated in Fig. 6.

3.4 STT test results

The sine-sweep test was first conducted to confirm the control effectiveness of the TMD with the designed parameters. The nacelle sine-sweep responses of the OWT model with and without the TMD are compared in Fig. 7. As shown in the figure, the time-history responses and the corresponding Fourier spectra reveal that the TMD could significantly reduce the OWT resonant response occurring around the fundamental frequency of the OWT. This behavior agreed with the design goal of the TMD. Therefore, the TMD parameters shown in Table 2 were considered applicable for the complete-model STT and the follow-up RTHT.

To further demonstrate the control performance of the TMD under seismic excitations, the time-history responses of the OWT model with and without the TMD subjected to the Hua-Lien (HWA062) and Chi-Chi (TCU102-NS) ground accelerations are compared in Figs. 8 and 9, respectively. As shown in the subplots (a) and (b) of both figures, the TMD was also effective in reducing the nacelle's acceleration and displacement responses under

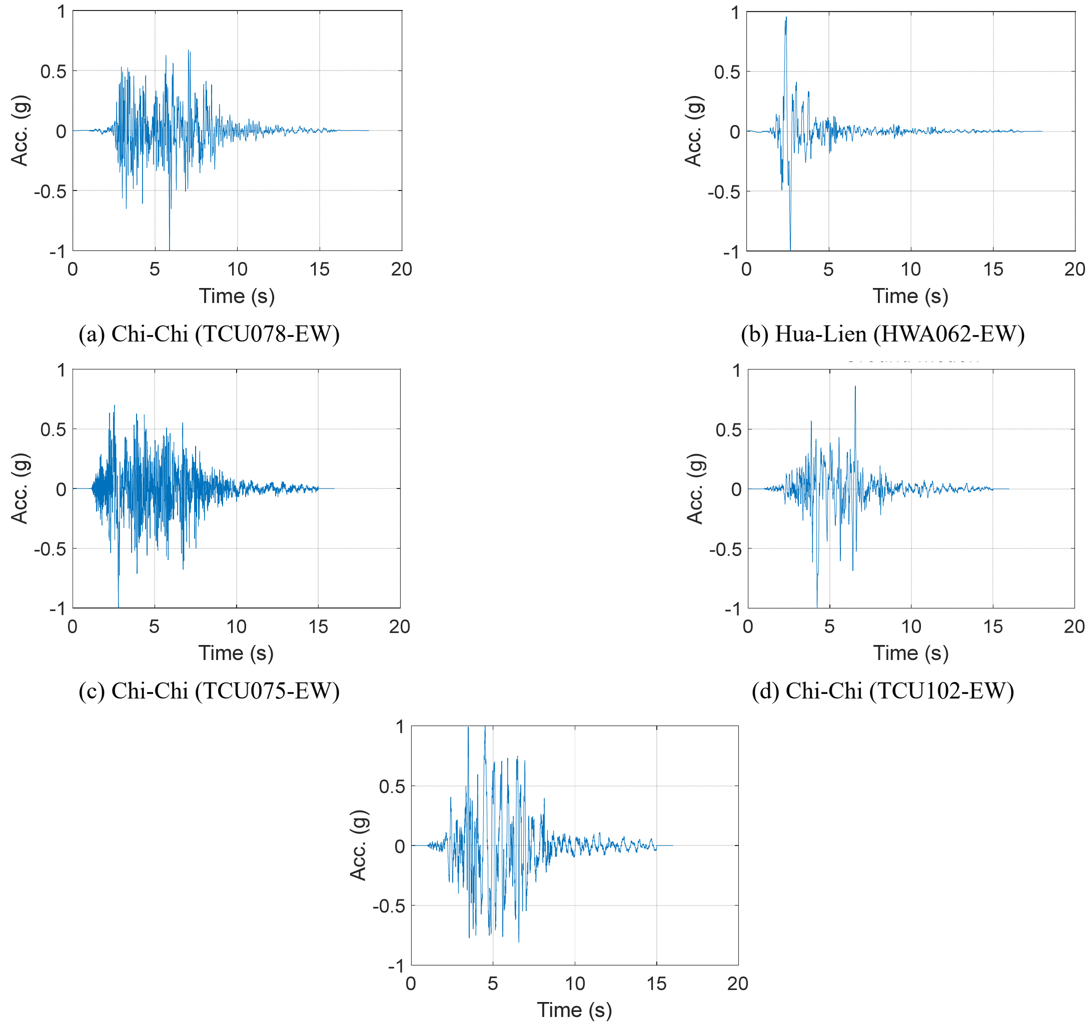

(a) Chi-Chi (TCU078-EW)

(b) Hua-Lien (HWA062-EW)

(c) Chi-Chi (TCU075-EW)

(d) Chi-Chi (TCU102-EW)

(e) Chi-Chi (TCU102-NS)

Fig. 6 Time histories of ground accelerations considered in the tests (PGA = 1.0 g)

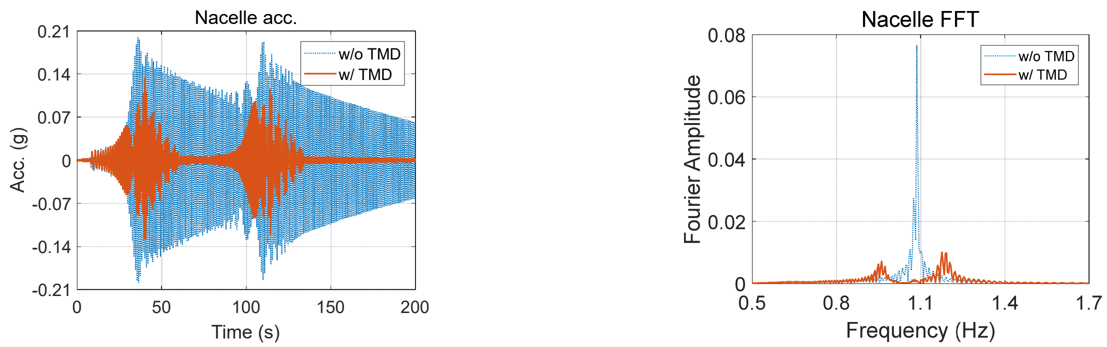

(a) Time-history of the nacelle acceleration

(b) Corresponding Fourier spectrum

Fig. 7 Control performance of TMD under a sine-sweep ground acceleration (0-2 Hz, PGA = 0.04 g)

earthquake excitations. The above STT test results were used to identify the system parameters of the numerical OWT model used in the RTHT. In addition, all STT test results served as the target responses in order to assess the accuracy of the RTHT, as discussed in a later section.

4. Identification of system parameters for the OWT numerical model

As mentioned above, in order to facilitate real-time control, the computational time in a RTHT has to be reduced, therefore to establish a simplified (reduced-order) OWT numerical model with less degrees of freedom, which

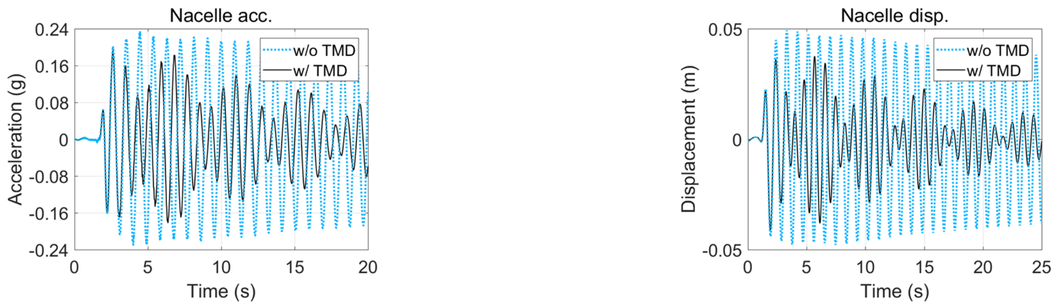

(a) Nacelle acceleration (b) Nacelle displacement

Fig. 8 Control performance of TMD under the HWA062-EW earthquake (PGA = 0.2 g)

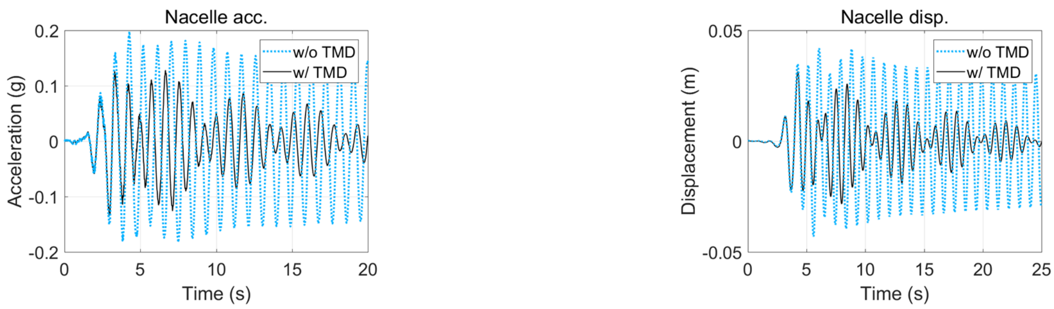

(a) Nacelle acceleration (b) Nacelle displacement

Fig. 9 Control performance of the TMD under the TCU102-NS earthquake (PGA = 0.1 g)

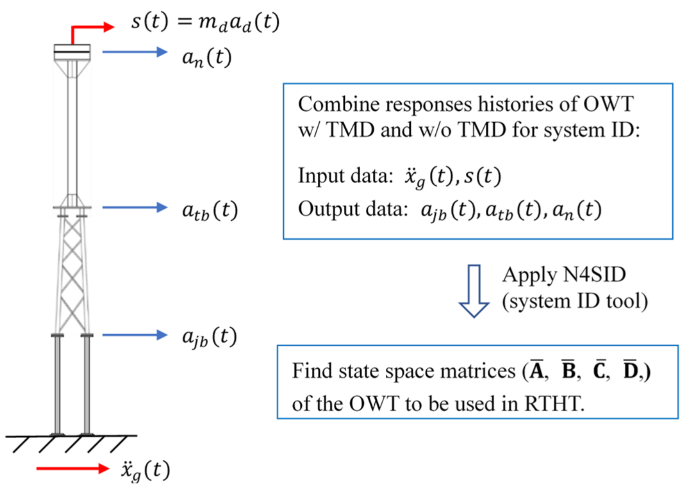

Fig. 10 System identification procedure for the OWT state-space model

is able to preserve the major dynamic characteristics of the OWT structure, is an important issue in the RTHT. For this reason, a general system identification procedure using the subspace identification (SID) technique is proposed in this section. The proposed procedure, applicable to any RTHT, may be applied in an experimental or a numerical way. Through the SID technique, the former is to identify the state-space matrices of the simplified numerical model by using the measured responses of an existing OWT structure (or prototype), while the latter is to identify the state-space matrices of the simplified model by using the simulated responses of a pre-established full finite-element model for the OWT structure.

Since this study aims to compare RTHT results with the experimental result of a STT, in which an OWT prototype has already been built, the simplified OWT numerical model will be identified using the dynamic response data of the OWT prototype measured in the STT, rather than using the simulated response of a finite-element model.

4.1 System identification procedure

In this section, the procedures used to identify the state-space matrices of the numerical OWT model to be used in the RTHT are discussed. As shown in Fig. 10, the acceleration time responses measured at specific locations on the OWT tested model w/ and w/o the TMD in the complete STT were firstly combined into data strings, and then, the MATLAB numerical tool for system identification, called the N4SID (subspace identification) algorithm (Overschee and Moor 1994), was employed to identify the corresponding state-space matrices (i.e., the $\bar{\boldsymbol{A}}$, $\bar{\boldsymbol{B}}$, $\bar{\boldsymbol{C}}$, and $\bar{\boldsymbol{D}}$ matrices in Eqs. (12) and (13)) for the numerical OWT model. As shown in Fig. 10, in the identification procedure, the input vector (excitation vector) $\mathbf{u}(t)$ consisted of the ground acceleration $\ddot{x}_g(t)$ and the TMD force $s(t)$ (see Eq. (8a)), while the output vector (observation vector) $\mathbf{y}$(t) consisted of the three acceleration responses (a_{jb}, a_{tb}, and a_n) observed at the jacket base, tower base, and nacelle, respectively (see Eq. (4)). With these input and output time-domain data, the N4SID numerical tool was able to identify the state-space matrices of the OWT. As shown in the Fourier spectrum in Fig. 4(a), the dynamic response of the OWT was mainly contributed by the first three translation modes, where the order of system matrix $\bar{\boldsymbol{A}}$ was taken to be 6 in the system identification process.

4.2 Identified state-space matrices

Following the procedure described above, the identified state-space matrices for the OWT model are all listed below

$$\bar{\mathbf{A}} = \begin{bmatrix} 0.062 & -2.821 & -23.037 & -5.394 & -1.912 & 0.764 \\ 2.726 & -0.029 & 33.854 & -4.100 & 4.668 & -1.777 \\ 23.017 & -34.100 & -0.366 & 1.096 & 0.363 & 3.474 \\ 5.374 & 4.064 & -1.254 & -0.016 & 0.274 & 1.342 \\ 2.058 & -4.607 & 0.220 & -0.157 & -0.548 & 115.393 \\ -0.663 & 2.037 & -2.473 & -1.196 & -114.756 & -0.464 \end{bmatrix} \tag{24}$$

$$\bar{\mathbf{B}} = \begin{bmatrix} -0.061 & -0.001 \\ -0.396 & 0.002 \\ -4.447 & 0.007 \\ -1.359 & 0.005 \\ -12.028 & 0.225 \\ 5.608 & -0.135 \end{bmatrix} \tag{25}$$

$$\bar{\mathbf{C}} = \begin{bmatrix} 4.493 & -5.700 & -0.860 & 0.110 & -0.217 & 1.254 \\ 6.407 & -7.125 & -1.857 & 0.122 & 0.120 & -1.252 \\ 4.877 & 3.365 & -0.400 & -0.168 & 0.066 & -0.127 \end{bmatrix} \tag{26}$$

$$\bar{\mathbf{D}} = \begin{bmatrix} 0 & 0.0021 \\ 0 & -0.0023 \\ 0 & 0.0016 \end{bmatrix} \tag{27}$$

The above state-space matrices were all identified based on the input vector $\mathbf{u}(t)$ and output vector $\mathbf{y}(t)$ given in metric units (SI units). The data for both vectors were taken from the complete STT. Notably, as discussed previously in Section 2.4, the identified state-space matrices may not have been unique for the OWT model due to coordinate transformation. However, because of the invariance in the transfer function matrix $\boldsymbol{G}(\omega)$, the identified state-space matrices are able to represent the OWT model, as long as the transfer functions resulting from these identified matrices are consistent with the tested model. To this end, the consistency between the OWT response predicted by the identified state-space matrices (see Eqs. (24)-(27)) and the experimental response measured in the complete STT are validated in the following subsections.

4.3 Frequency-domain response validation

Due to the dimensions of the identified state-space matrices given in Eqs. (24)-(27), the corresponding transfer function matrix $\boldsymbol{G}(\omega)$, determined via Eq. (10), has a dimension of (3 × 2), i.e., 2 inputs and 3 outputs; therefore, Eq. (9) can be written explicitly as

$$\begin{Bmatrix} Y_1(\omega) \\ Y_2(\omega) \\ Y_3(\omega) \end{Bmatrix} = \begin{bmatrix} G_{11}(\omega) & G_{12}(\omega) \\ G_{21}(\omega) & G_{22}(\omega) \\ G_{31}(\omega) & G_{32}(\omega) \end{bmatrix} \begin{Bmatrix} U_1(\omega) \\ U_2(\omega) \end{Bmatrix} \tag{28}$$

where $G_{ij}(\omega)$ physically represents the transfer function of the i^{th} output $Y_i(\omega)$ due to the j^{th} input $U_i(\omega)$. The value of each transfer function $U_{ij}(\omega)$ can be determined numerically via Eq. (10) and Eqs. (24)-(27). The inputs $U_1(\omega)$ and $U_2(\omega)$ represent the Fourier transforms of $\ddot{x}_g(t)$ and $s(t)$ (see Eq. (8a)), respectively, while outputs $Y_1(\omega)$, $Y_2(\omega)$, and $Y_3(\omega)$ represent the Fourier transforms of a_{jb}, a_{tb}, and a_n (see Eq. (4)), i.e., the acceleration responses at the jacket base, tower base, and nacelle, respectively. Basically, Eq. (28) states that once the transfer function $U_{ij}(\omega)$ is determined, the Fourier responses $Y_i(\omega)$ (i = 1, 2, 3) of the OWT tested model can be predicted for any given inputs $U_i(\omega)$ (i = 1, 2). Under the Chi-Chi (TCU078, PGA = 0.2 g) earthquake conditions, Fig. 11 compares the predicted Fourier responses $Y_i(\omega)$ of the nacelle, tower base, and jacket base with those obtained from the experimental data from the complete STT. In the figure, the predicted $Y_i(\omega)$ (i = 1, 2, 3) are computed using Eq. (28), with matrix $\boldsymbol{G}(\omega)$ constructed from the identified state-space matrices, and the inputs being the Fourier transforms of $\ddot{x}_g(t)$ and $s(t)$ measured in the STT; while the experimental $Y_i(\omega)$ (i = 1, 2, 3) are obtained by taking the Fourier transforms of the measured a_{jb}, a_{tb}, and a_n.

Fig. 11 shows favorable agreement between the predicted and experimental results for the Fourier amplitude and the phase plots. This consistency indicates that the computed transfer function matrix $\boldsymbol{G}(\omega)$ is accurate enough for the tested OWT model. More importantly, due to the invariance in the transfer function matrix, the set of the state-space matrices in Eqs. (24)-(27) is feasible and is also accurate enough to serve as a numerical model for the OWT substructure in the RTHT, for which the test results are reported in the next section. Fig. 11(a) also shows that the identified state-space model can simulate the interaction behavior between the OWT and the TMD since two closely spaced peaks can be clearly observed in the amplitude plot.

4.4 Time-domain response validation

In Fig. 12, under the Chi-Chi (TCU078-EW) ground motion (PGA = 0.2 g) condition, the experimental accelerations at the jacket base, tower base, and nacelle of the OWT tested model with the TMD are compared with

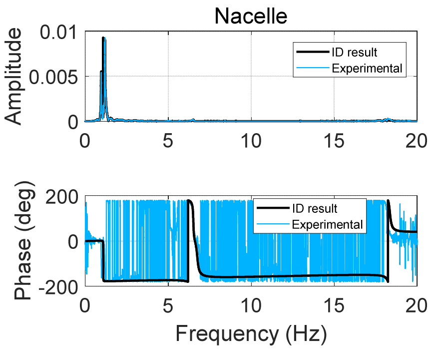

(a) Nacelle acceleration

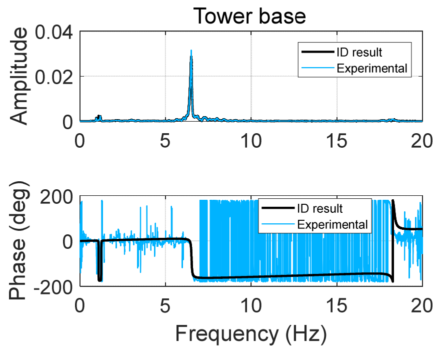

(b) Tower-base acceleration

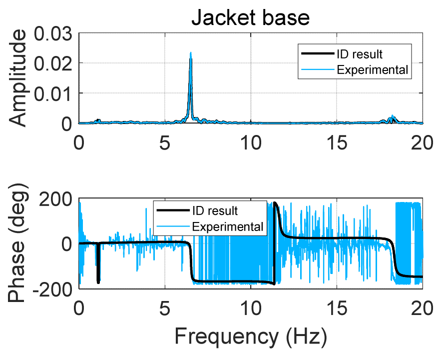

(c) Jacket-base acceleration

Fig. 11 Comparison of measured and identified transfer functions for the OWT-TMD system (TCU078-EW, PGA = 0.2 g)

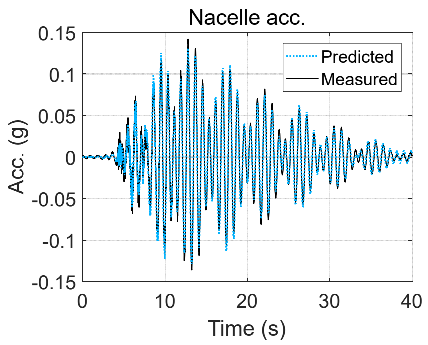

(a) Nacelle acceleration

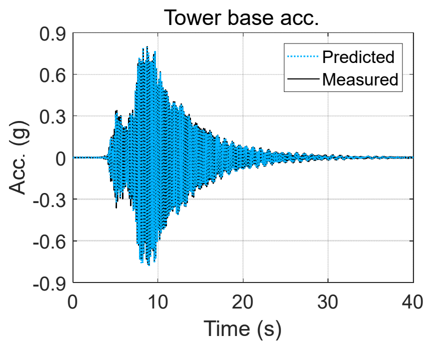

(b) Tower-base acceleration

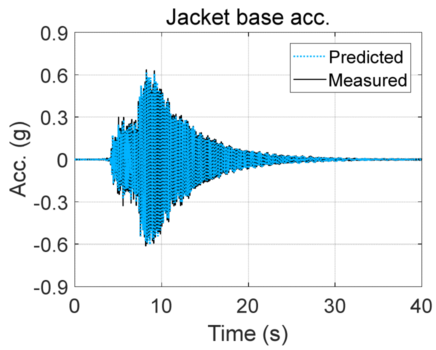

(c) Jacket-base acceleration

Fig. 12 Comparison of the measured and predicted responses of the OWT-TMD system (TCU078-EW, PGA = 0.2 g)

the predicted responses simulated using the identified state-space matrices. In the figure, the predicted responses are simulated with Eqs. (12) and (13) using the ground acceleration $\ddot{x}_g(t)$ and the TMD force $s(t)$ (see Eq. (3)) measured from the STT as the input vector $\mathbf{u}(t)$. Fig. 12 demonstrates that the identified state-space matrices are

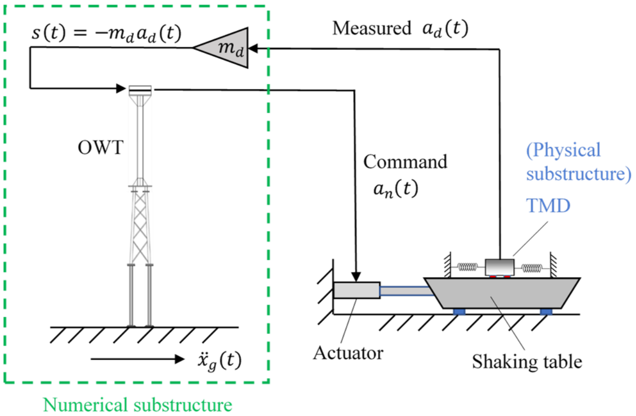

Fig. 13 Framework of the RTHT

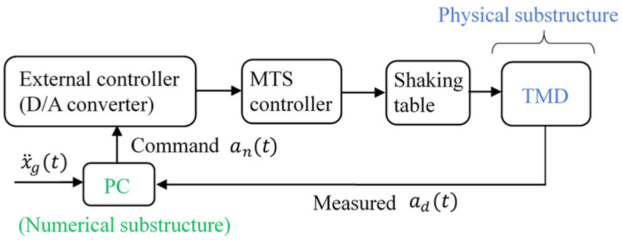

Fig. 14 Control flowchart of the RTHT

able to accurately simulate the OWT acceleration responses at the various elevations of interest, i.e., the locations of the nacelle, tower base, and jacket base.

5. Real-time hybrid test for the OWT with a TMD

5.1 Test setup of RTHT

The framework of the RTHT in this study is shown schematically in Fig. 13, while the control flow chart of the RTHT is shown in Fig. 14. As shown in Fig. 13, in the RTHT, the complete OWT-TMD system (see Fig. 1(a)) was divided into a numerical and a physical substructure. The numerical substructure represented the OWT with the jacket structure, while the physical substructure was the TMD. As shown in Fig. 13, the OWT numerical substructure, whose response was numerically simulated by the state-space model (a 3-DOF system) identified in Section 4.2, was implemented in Matlab-Simulink software. Fig. 3 shows a photo of the RTHT test setup. As shown in Fig. 3, the physical substructure, i.e., the TMD specimen, was directly mounted on the shaking table, and the relative displacement and the absolute acceleration $a_d(t)$ of the TMD mass block were measured with a displacement meter and an accelerometer, respectively. The shaking table in the RTHT was used to physically simulate the motion of the OWT nacelle on which the TMD was installed. As shown in Fig. 13, when conducting the RTHT, the numerical OWT model was excited numerically by both the ground acceleration $\ddot{x}_g(t)$ and the interaction force $s(t)$, which was computed via Eq. (3) with the measured TMD's acceleration $a_d(t)$. As shown in Fig. 14, the numerically simulated nacelle acceleration $a_n(t)$ of the OWT was then taken to be the command to control the shaking table through a D/A converter and the MTS controller. Then, the TMD acceleration $a_d(t)$ was measured and used to calculate the next time-step OWT response.

5.2 Frequency response of the shaking table control system

Because the dynamic property and control performance of the shaking table significantly affect the RTHT results, a system identification test was conducted to investigate the transfer function of the 8×8 m shaking table in the NCREE's Tainan Laboratory. In that test, the shaking table was excited with a white noise input command, and the control command and table acceleration feedback were recorded simultaneously. Fig. 15(a) shows the time histories of the table's command and feedback signals, while Fig. 15(b) depicts the transfer function of the shaking table, which is equal to the ratio of the Fourier spectrum of the feedback signal to the Fourier spectrum of the command. The amplitude plot in Fig. 15(b) shows that the shaking table was able to closely follow the control command within 0-50 Hz, while the phase angle plot indicates that the control delay time was only approximately 0.01s since the predicted frequency for 360 degrees of the phase lag was approximately 100 Hz.

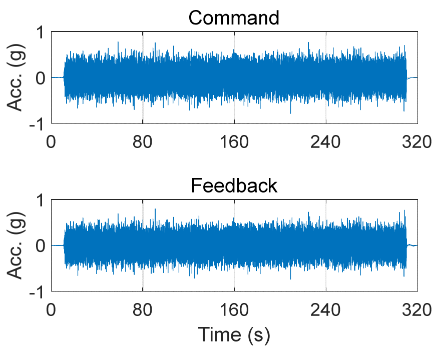

(a) Command and feedback signals

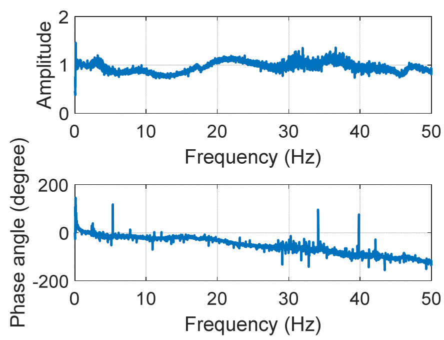

(b) Transfer function

Fig. 15 Transfer function of the shaking table under the external control mode

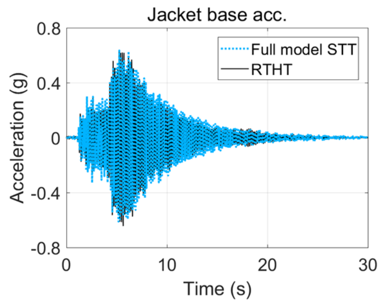

(a) Jacket-base acceleration

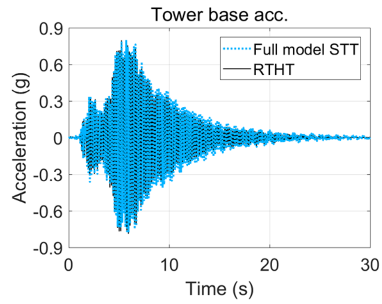

(b) Tower-base acceleration

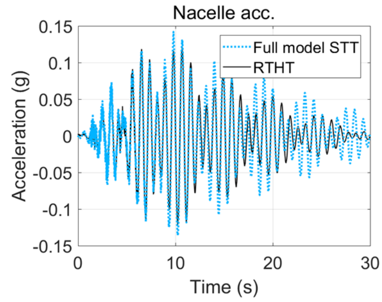

(c) Nacelle acceleration

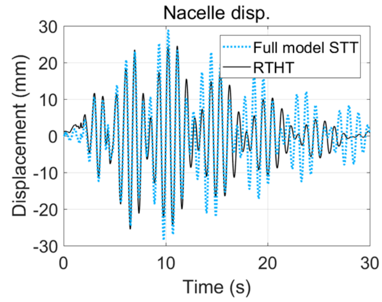

(d) Nacelle displacement

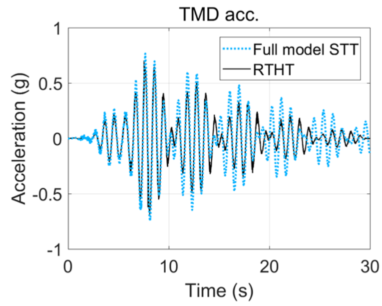

(e) TMD acceleration

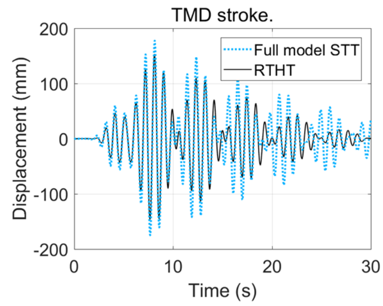

(f) TMD stroke

Fig. 16 Comparison of the RTHT (with the MDOF model) and STT responses (TCU078-EW, PGA = 0.2 g)

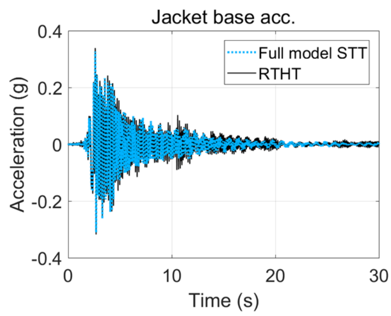

(a) Jacket-base acceleration

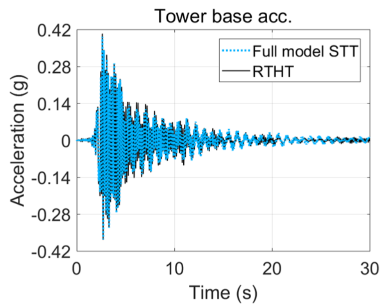

(b) Tower-base acceleration

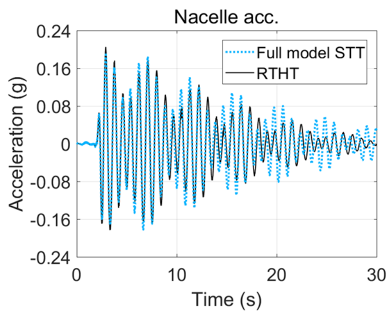

(c) Nacelle acceleration

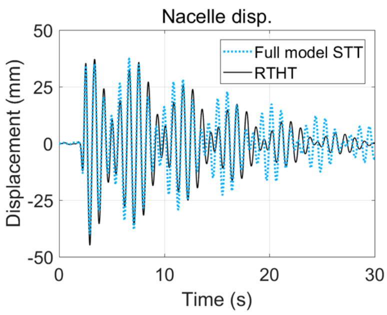

(d) Nacelle displacement

Fig. 17 Comparison of the RTHT (with the MDOF model) and STT responses (HWA062-EW, PGA = 0.2 g)

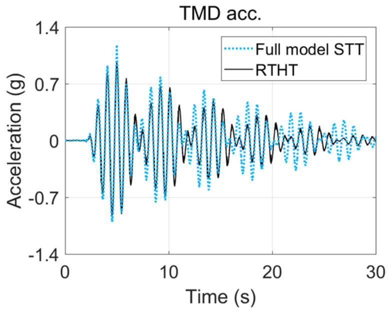

(e) TMD acceleration

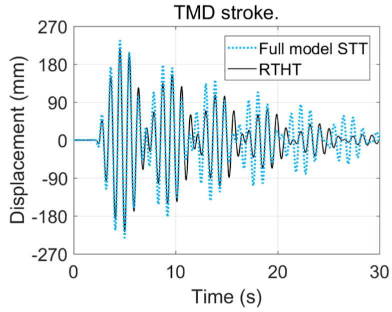

(f) TMD stroke

Fig. 17 Continued

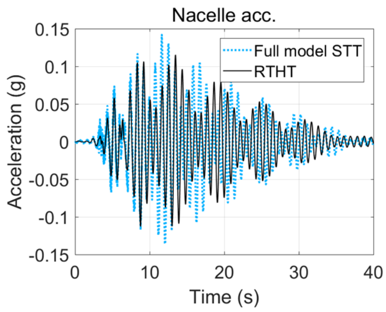

(a) Nacelle acceleration

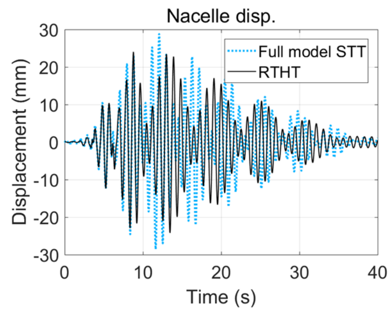

(b) Nacelle displacement

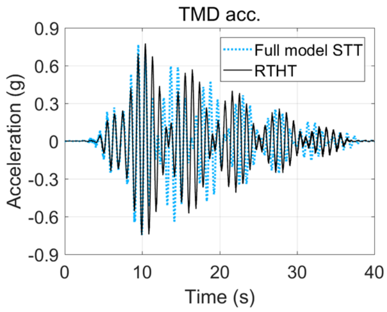

(c) TMD acceleration

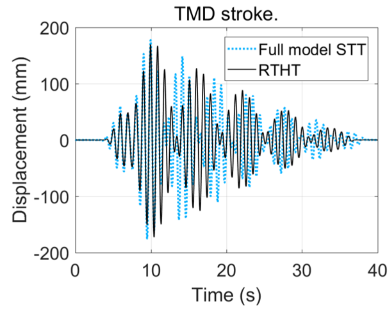

(d) TMD stroke

Fig. 18 Comparison of the RTHT (with the SDOF model) and STT responses (TCU078-EW, PGA = 0.2 g)

5.3 Comparison of the RTHT and STT results

To show the accuracy of the RTHT, Figs. 16 and 17 compare the experimental results for the RTHT (with the MDOF OWT model) with those measured in the complete STT (the test with the complete model), under the Chi-Chi (TCU078-EW) and Hua-Lien (HWA062-EW) earthquake conditions with a PGA = 0.2 g, respectively. Each of Figs. 16 and 17 contains six subfigures. Subfigures (a), (b), and (c) compare the accelerations of the jacket base, tower base, and nacelle, respectively. The RTHT results in these three subfigures were generated on-line using the numerical OWT for which the state-space matrices (a 3-DOF system) were identified in Section 4.2. Notably, the nacelle acceleration in Subfigure (c) was also used as the control command of the shaking table in the RTHT. Subfigure (d) compares the nacelle's displacement, while subfigures (e) and (f) compare the TMD's acceleration and stroke. The RTHT results shown in subfigures (d), (e), and (f) are the measured responses of the physical substructure in the RTHT. The STT results in all the subfigures are the measured responses. The results of the comparison shown in Figs. 16 and 17 indicate that the seismic responses of the OWT-TMD system obtained from the RTHT generally agree with those of the STT, especially around the main shock of the earthquakes. This demonstrates that the RTHT is able to reproduce seismic responses at various spots on the OWT structure. Therefore, the feasibility and accuracy of the RTHT were both verified.

5.4 Comparison of RTHT accuracy for different OWT numerical models

Generally, in a TMD parameter design, the primary structure to be controlled is simplified as a single degree of freedom (SDOF) system (Lin *et al*. 1994). Therefore, in most previous TMD studies involving RTHTs, the primary structures were modelled numerically using an SDOF system (Chu *et al*. 2018). Nevertheless, for a complicated structural system, such as the OWT with a jacket-type

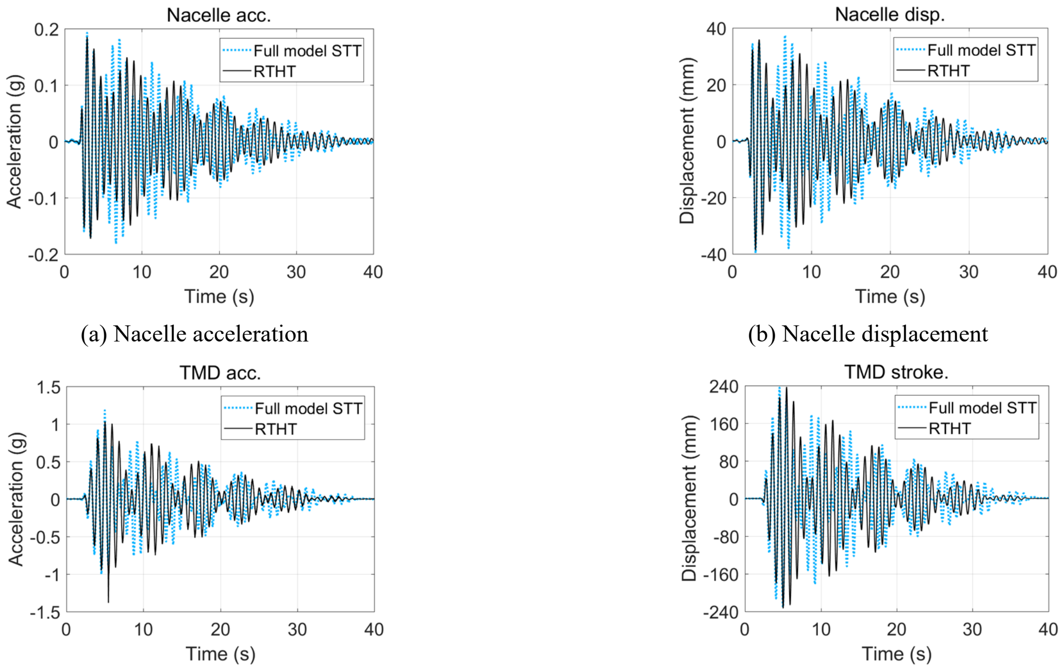

(a) Nacelle acceleration (b) Nacelle displacement

(c) TMD acceleration (d) TMD stroke

Fig. 19 Comparison of the RTHT (with the SDOF model) and STT responses (HWA062-EW, PGA = 0.2 g)

supporting structure considered in this study, an SDOF numerical model may inevitably induce a greater amount of modelling error. To evaluate the accuracy of the RTHT with different numerical models, in this study, the RTHT of the OWT-TMD system using an SDOF-OWT numerical model (hereafter, called the RTHT(SDOF) model) was also tested, and its results were compared with those when using the MDOF-OWT model (hereafter, called the RTHT(MDOF) model) presented in Section 5.3. In the tests, the structural parameters listed in Table 1 and Eqs. (24)-(27) were adopted for the RTHT(SDOF) and RTHT(MDOF) models, respectively.

The time-history responses of the RTHT(MDOF) presented in Figs. 16 and 17, and those in Figs. 18 and 19 compare the responses of the RTHT(SDOF) with those of the complete STT under the Chi-Chi (TCU078-EW) and Hua-Lien (HWA062-EW) earthquake conditions at PGA = 0.2 g, respectively. In these two figures, subfigures (a) and (b) compare the nacelle's acceleration and displacement responses, while subfigures (c) and (d) compare the measured TMD's acceleration and stroke.

Figs. 18 and 19 indicate that although the RTHT using the simple SDOF model can capture the main-shock responses of the nacelle and TMD, it may also lose accuracy in terms of the follow-up free-vibration responses, as compared with the RTHT(MDOF) (see Figs. 16 and 17). More importantly, due to the model's limitations, only the response for the nacelle could be obtained in the RTHT(SDOF), and the responses of the tower and jacket were completely absent.

To further quantify the accuracy of the RTHT results, in Fig. 20, the peak responses of the nacelle and TMD obtained from the RTHT(SDOF) and RTHT(MDOF) are compared with those of the complete STT. A total of nine ground accelerations with the different PGA levels listed in Table 3 were considered in all three tests. In the four subfigures shown in Fig. 20, the horizontal axis represents the peak response of the STT (with the full model), while the vertical axis represents the peak responses of the RTHT(MDOF) and RTHT(SDOF). The percentage lines shown in the subfigures represent the ratio of the RTHT result to the STT result. A data point on the diagonal line implies that the corresponding RTHT response completely matches that of the STT under the same ground excitation; therefore, the closer the data point is to the diagonal line, the more accurate the RTHT is.

Fig. 20 indicates that the RTHTs with both the SDOF and MDOF numerical models can predict the peak responses of the nacelle and TMD with the same accuracy. Generally speaking, with the exception of the nacelle displacement, all the peak responses for both RTHTs deviate from those of the STT by around $\pm 10\%$. The RTHT's nacelle displacement, which was obtained physically by measuring the shaking table displacement, has a higher amount of deviation in some ground excitations because the RTHTs were determined through the acceleration control of the shaking table, which may have resulted in the loss of some displacement accuracy.

Furthermore, in order to measure the over-all accuracy of the time-history responses predicted by the RTHTs, in addition to the accuracy of the peak responses, a root-mean-square (RMS) error index ε_{RMS} for both the RTHT(MDOF) and RTHT(SDOF) is also defined below as

$$\varepsilon_{RMS} = \sqrt{\frac{\sum_{i=1}^{N}\left(x_{RTHT}(i) - x_{STT}(i)\right)^2}{N}} \tag{29}$$

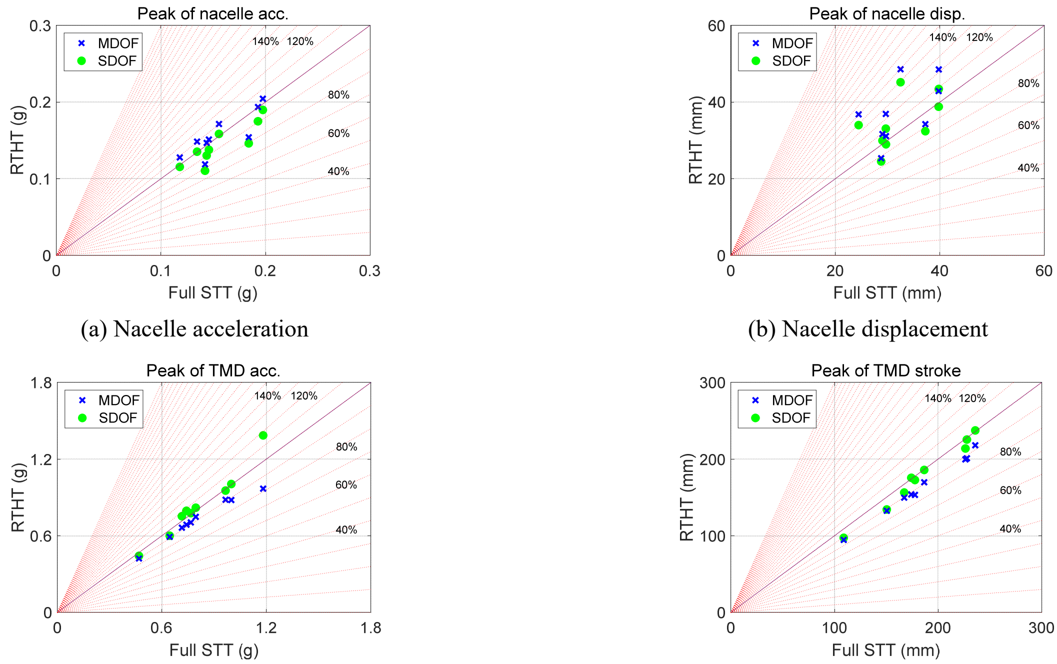

(a) Nacelle acceleration (b) Nacelle displacement

(c) TMD acceleration (d) TMD stroke

Fig. 20 Comparison of peak responses of the RTHTs with different numerical models

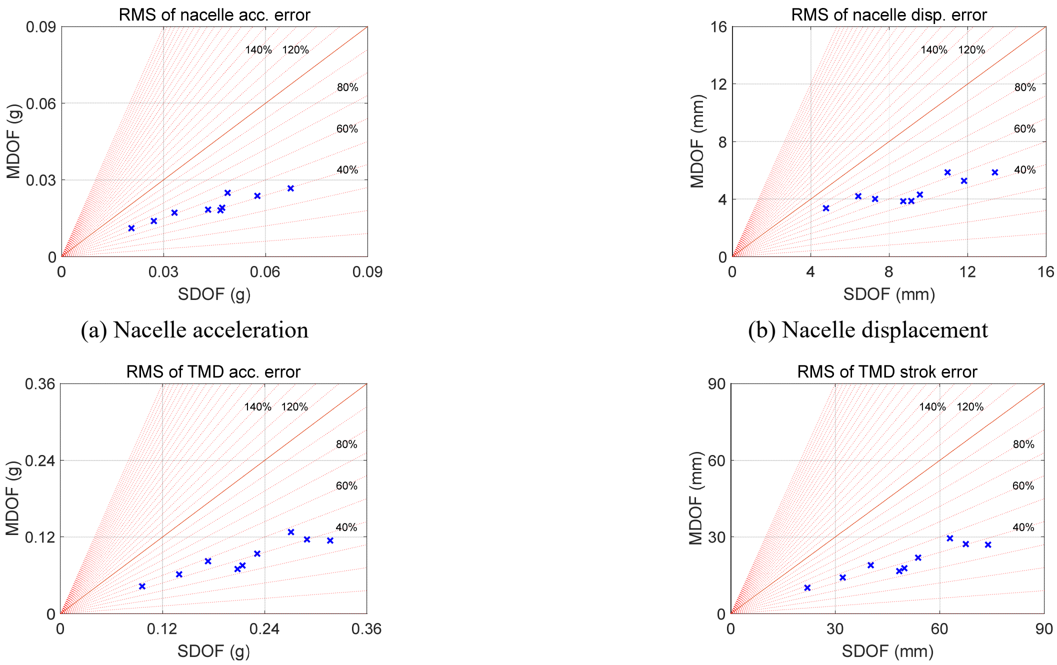

(a) Nacelle acceleration (b) Nacelle displacement

(c) TMD acceleration (d) TMD stroke

Fig. 21 Comparison of RMS errors in the RTHTs with different numerical models

where N denotes the total number of data points, and $x_{RTHT}(i)$ and $x_{STT}(i)$ represent the response values of the RTHT and STT measured at the i-th time step, respectively. In the four subfigures shown in Fig. 21, the RMS errors in the acceleration and displacement responses of the nacelle and TMD for both RTHTs are compared. In each subfigure, the horizontal and vertical axes represent the RMS errors for the RTHT(SDOF) and RTHT(MDOF), respectively. Therefore, a data point on the diagonal line implies that both RTHTs have an equal amount of RMS error under the same ground motion. The percentage lines shown in the subfigures represent the ratio of the RMS error of the RTHT(MDOF) to that of the RTHT(SDOF).

As shown in Fig. 21, all the data points in the four subfigures fall on the right side of the diagonal lines, indicating that the RMS error for the RTHT(MDOF) is lower than that for the RTHT(SDOF) under all types of ground excitation. The RTHT(MDOF) model can reduce the RMS error by approximately 40-60% as compared to the RTHT(SDOF) model.

Therefore, the RTHT using an MDOF numerical model is much more accurate in terms of predicting the over-all time-history responses of the nacelle and TMD in an OWT-TMD system as compared to those predicted using an SDOF model.

5. Conclusions

A real-time hybrid test (RTHT) can be an effective means by which to test the control effectiveness of a tuned mass damper (TMD) employed to suppress the seismic responses of an off-shore wind turbine (OWT) structure. In order to access the accuracy and reliability of the RTHT for an OWT-TMD system with a complicated jacket-type supporting structure, in this study, the results of the RTHT were compared with those obtained using a shaking table test (STT) with a complete tested model. In the STT, a 1/25-scale OWT-TMD model, whose parameters were determined according to a typical 5-MW OWT with a jacket structure, was constructed and dynamically tested. On the other hand, in the RTHT, the 1/25-scale OWT-TMD model was substructured, such that only the TMD was physically tested, and the OWT was numerically simulated using a simplified SDOF model and a multiple-DOF (MDOF) model whose state-space matrices were identified experimentally considering the OWT-TMD interaction effect. It was further proven that the identified state-space model could accurately simulate the dynamic behavior of the OWT-TMD system in either the time domain or frequency domain. Then, the test results of the RTHTs with the simplified SDOF and the MDOF OWT models were compared with those obtained from the STT. The comparison revealed that both the SDOF and the MDOF models can predict the peak responses of the nacelle and TMD well. However, while the RTHT with the SDOF model requires less on-line control computational time, the MDOF model is more accurate in terms of predicting the over-all time-history responses of the nacelle and TMD. Therefore, an MDOF OWT model should be employed in an RTHT for an OWT-TMD system if the accuracy of the response history is a concern. In addition, while the SDOF model can only predict structural responses at a specific location (e.g., the top of the OWT), the RTHT with the MDOF model can predict seismic responses at multiple critical locations on the OWT structure. It is thus concluded that, compared with a shaking table test, the RTHT is a reliable and cost-effective alternative to assess the control performance of the TMD for an OWT, and depending on the types of structural responses considered, either an SDOF or a MDOF numerical model can be adopted in the RTHT, provided that the primary dynamic characteristics of the OWT structure can be accurately captured using the numerical model.

Acknowledgments

The authors thank the Tainan laboratory at the National Center for Research on Earthquake Engineering (NCREE, Taiwan) for technical and financial support for the experiments. The authors are also grateful to Prof. Chi-Chang Lin (the Department of Civil Engineering, National Chung Hsing University, Taiwan) for the valuable information related to the design and fabrication of the TMD system.

References

Asai, T., Chang, C.M. and Spencer Jr., B.F. (2015), "Real-time hybrid simulation of a smart base-isolated building", *J. Eng. Mech.*, **141**(3), 1943-7889. https://doi.org/10.1061/(ASCE)EM.1943-7889.0000844

Bargi, K., Dezvareh, R. and Mousavi, S.A. (2016), "Contribution of tuned liquid column gas dampers to the performance of offshore wind turbines under wind, wave, and seismic excitations", *Earthq. Eng. Eng. Vib.*, **15**, 551-561. https://doi.org/10.1007/s11803-016-0343-z

Calabrese, A., Strano, S. and Terzo, M. (2015), "Real-time hybrid simulations vs shaking table tests: Case study of a fibre-reinforced bearings isolated building under seismic loading", *Struct. Control. Health. Monitor.*, **22**(3), 535-556. https://doi.org/10.1002/stc.1687

Carrion, J.E. and Spencer Jr., B.F. (2008), "Real-time hybrid testing using model-based delay compensation", *Smart Struct. Syst., Int. J.*, **4**(6), 809-828. https://doi.org/10.12989/sss.2008.4.6.809

Chae, Y., Park, M., Kim, C.Y. and Park, Y.S. (2017), "Experimental study on the rate-dependency of reinforced concrete structures using slow and real-time hybrid simulations", *Eng. Struct.*, **132**, 648-658. https://doi.org/10.1016/j.engstruct.2016.11.065

Chang, S.Y., Wu, T.H., Tran, N.C. and Yang, Y.S. (2017), "Applications of a family of unconditionally stable, dissipative, explicit methods to pseudo dynamic tests", *Experim. Techniq.*, **41**(1), 19-36. https://doi.org/10.1007/s40799-016-0151-4

Chen, J. and Georgakis, C.T. (2013), "Tuned rolling-ball dampers for vibration control in wind turbines", *J. Sound Vib.*, **332**(21), 5271-5282. https://doi.org/10.1016/j.jsv.2013.05.019

Chen, P.C., Tsai, K.C. and Lin, P.Y. (2014), "Real-time hybrid testing of a smart base isolation system", *Earthq. Eng. Struct. Dyn.*, **43**(1), 139-158. https://doi.org/10.1002/eqe.2341

Chen, P.C., Chang, C.M., Spencer Jr., B.F. and Tsai, K.C. (2015), "Adaptive model-based tracking control for real-time hybrid simulation", *Bull. Earthq. Eng.*, **13**, 1633-1653. https://doi.org/10.1007/s10518-014-9681-2

Chen, P.C., Hsu, S.C., Zhong, Y.J. and Wang, S.J. (2019), "Realtime hybrid simulation of smart base-isolated raised floor systems for high-tech industry", *Smart Struct. Syst., Int. J.*, **23**(1), 91-106. https://doi.org/10.12989/sss.2019.23.1.091

Chen, P.C., Dong, M.W., Chen, P.C. and Nakata, N. (2020), "Stability analysis and verification of real-time hybrid simulation using a shake table for building mass damper systems", *Front. Built Environ.*, **6**, 109. https://doi.org/10.3389/fbuil.2020.00109

Chu, S.Y., Lu, L.Y., Yeh, S.W., Chia, P.Y. and Ning, W.C. (2018), "Real-time hybrid testing of a structure with a piezoelectric friction controllable mass damper by using a shake table", *Struct. Control. Health. Monitor.*, **25**(3), e2124. https://doi.org/10.1002/stc.2124

Colwell, S. and Basu, B. (2009), "Tuned liquid column dampers in offshore wind turbines for structural control", *Eng. Struct.*,

31(2), 358-368. https://doi.org/10.1016/j.engstruct.2008.09.001

Connor, J.J. (2002), *Introduction to Structural Motion Control*., 1st edition, Prentice Hall.

Drazina, P.L. and Govindjee, S. (2017), "Hybrid simulation theory for a classical nonlinear dynamical system", *J. Sound Vib.*, **3927**, 240-259. https://doi.org/10.1016/j.jsv.2016.12.034

Facchinetti, A. and Bruni, S. (2012), "Hardware-in-the-loop hybrid simulation of pantograph–catenary interaction", *J. Sound Vib.*, **331**(12), 2783-2797. https://doi.org/10.1016/j.jsv.2012.01.033

Fu, B., Jiang, H. and Wu, T. (2019), "Experimental study of seismic response reduction effects of particle damper using substructure shake table testing method", *Struct. Control Health Monitor.*, **26**(2), e2295. https://doi.org/10.1002/stc.2295

Hakuno, H., Shidawara, M. and Hara, T. (1969), "Dynamic destructive test of a cantilever beam controlled by an analog-computer", *Transact. Japan Soc. Engr.*, **171**, 1-9. https://doi.org/10.2208/jscej1969.1969.171_1

Hayati, S. and Song, W. (2017), "An optimal discrete-time feedforward compensator for real-time hybrid simulation", *Smart Struct. Syst., Int. J.*, **20**(4), 483-498. https://doi.org/10.12989/sss.2017.20.4.483

He, T. and Jiang, N. (2019), "Substructure shake table test for equipment-adjacent structure-soil interaction based on the branch mode method", *Struct. Des. Tall Spec. Build.*, **28**(4), e1573. https://doi.org/10.1002/tal.1573

Horiuchi, T., Inoue, M., Konno, T. and Namita, Y. (1999), "Real-time hybrid experimental system with actuator delay compensation and its application to a piping system with energy absorber", *Earthq. Eng. Struct. Dyn.*, **28**(10), 1121-1141. https://doi.org/10.1002/(SICI)1096-9845(199910)28:10<1121::AID-EQE858>3.0.CO;2-O

Horiuchi, T., Inoue, M. and Konno, T. (2000), "Development of a real-time hybrid experimental system using a shaking table", *Proceedings of the 12th World Conference on Earthquake Engineering*, Auckland, New Zealand.

Iemura, H., Igarashai, A. and Takahashi, Y. (1999), "Sub-structured hybrid techniques for actuator loading and shake table tests", *Proceedings of the First International Conference on Advances in Structural Engineering and Mechanics*, Seoul, South Korea.

Igarashi, A., Iemura, H. and Suwa, T. (2000), "Development of sub-structured shaking table test method", *Proceedings of the 12th World Conference on Earthquake Engineering*, Auckland, New Zealand.

Igarashi, A., Iemura, H., Tanaka, H. and Tsuruta, D. (2004), "Experimental simulation of coupled response of structural systems using the substructure hybrid shake table test method", *Proceedings of the 13th World Conference on Earthquake Engineering*, Vancouver, Canada.

Jin, X., Xie, S., He, J., Lin, Y., Wang, Y. and Wang, N. (2018), "Optimization of tuned mass damper parameters for floating wind turbines by using the artificial fish swarm algorithm", *Ocean Eng.*, **167**, 130-141. https://doi.org/10.1016/j.oceaneng.2018.08.031

Jonkman, J., Butterfield, S., Musial, W. and Scott, G. (2009), "Definition of a 5-MW reference wind turbine for offshore system development", National Renewable Energy Laboratory; NREL/TP-500-38060.

Ju, S.H. and Huang, Y.C. (2019), "Analyses of offshore wind turbine structures with soil-structure interaction under earthquakes", *Ocean Eng.*, **187**, 106190. https://doi.org/10.1016/j.oceaneng.2018.08.031

Ju, S.H., Su, F.C., Jiang, Y.T. and Chiu, T.C. (2019a), "Ultimate load design of jacket-type offshore wind turbines under tropical cyclones", *Wind Energy*, **22**(5), 685-697. https://doi.org/10.1002/we.2315

Ju, S.H., Su, F.C., Ke, Y.P. and Xie, M.H. (2019b), "Fatigue design of offshore wind turbine jacket-type structures using a parallel scheme", *Renew. Energy*, **136**, 69-78. https://doi.org/10.1016/j.renene.2018.12.071

Khoo, H.H., Tsai, K.C., Tsai, C.Y., Tsai, C.Y. and Wang, K.J. (2016), "Bidirectional substructure pseudo-dynamic tests and analysis of a full-scale two-story buckling-restrained braced frame", *Earthq. Eng. Struct. Dyn.*, **45**(7), 1085-1107. https://doi.org/10.1002/eqe.2696

Lackner, M.A. and Rotea, M.A. (2011), "Passive structural control of offshore wind turbines", *Wind Energy*, **14**(3), 373-388. https://doi.org/10.1002/we.426

Lee, S.K., Park, E.C., Min, K.W., Lee, S.H., Chung, L. and Park, J.H. (2007), "Real-time hybrid shaking table testing method for the performance evaluation of a tuned liquid damper controlling seismic response of building structures", *J. Sound Vib.*, **302**(3), 596-612. https://doi.org/10.1016/j.jsv.2006.12.006

Li, J., Zhang, Z. and Chen, J. (2012), "Experimental study on vibration control of offshore wind turbines using a ball vibration absorber", *Energy Power Eng.*, **4**(3), 153-157. https://doi.org/10.4236/epe.2012.43021

Lin, C.C., Hu, C.M., Wang, J.F. and Hu, R.Y. (1994), "Vibration control effectiveness of passive tuned mass dampers", *J. Chin. Inst. Eng.*, **17**(3), 367-376. https://doi.org/10.1080/02533839.1994.9677600

Lin, C.C., Ueng, J.M. and Huang, T.C. (1999), "Seismic response reduction of irregular buildings using passive tuned mass dampers", *Eng. Struct.*, **22**(5), 513-524. https://doi.org/10.1016/S0141-0296(98)00054-6

Lin, G.L., Lu, L.Y., Lei, K.T., Liu, K.Y., Ko, Y.Y. and Ju, S.H. (2021), "Experimental study on seismic vibration control of an offshore wind turbine with TMD considering soil liquefaction effect", *Mar. Struct.*, **77**, 102961. https://doi.org/10.1016/j.marstruc.2021.102961

Ljung, L. (1999), *System identification: Theory for the user*, 2nd ed., Prentice Hall, Englewood Cliffs, NJ, USA.

Lu, L.Y., Lin, G.L. and Lin, C.Y. (2011), "Experimental verification of a piezoelectric smart isolation system", *Struct. Control Health Monitor.*, **18**(8), 869-889. https://doi.org/10.1002/stc.407

Lu, L., Fermandois, G.A., Lu, X., Spencer Jr., B.F., Duan, Y.F. and Zhou, Y. (2019), "Experimental evaluation of an inertial mass damper and its analytical model for cable vibration mitigation", *Smart Struct. Syst., Int. J.*, **23**(6), 589-613. https://doi.org/10.12989/sss.2019.23.6.589

Mahin, S.A. and Shing, P.B. (1985), "Pseudo dynamic method for seismic testing", *J. Struct. Eng.*, **111**(7), 1482-1503. https://doi.org/10.1061/(ASCE)0733-9445(1985)111:7(1482)

McCrum, D.P. and Williams, M.S. (2016), "An overview of seismic hybrid testing of engineering structures", *Eng. Struct.*, **118**, 240-261. https://doi.org/10.1016/j.engstruct.2016.03.039

Nakashima, M., Kato, H. and Takaoka, E. (1992), "Development of real-time pseudo dynamic testing", *Earthq. Eng. Struct. Dyn.*, **21**(1), 79-92. https://doi.org/10.1002/eqe.4290210106

Neild, S.A., Stoten, D.P., Drury, D. and Wagg, D.J. (2005), "Control issues relating to real-time sub-structuring experiments using a shaking table", *Earthq. Eng. Struct. Dyn.*, **34**(9), 1171-1192. https://doi.org/10.1002/eqe.473

Overschee, P.V. and Moor, B.D. (1994), "N4SID: Subspace algorithms for the identification of combined deterministic-stochastic systems", *Automatica*, **30**(1), 75-93. https://doi.org/10.1016/0005-1098(94)90230-5

Reinhorn, A.M., Bruneau, M., Chu, S.Y., Shao, X. and Pitman, M.C. (2003), "Large scale real time dynamic hybrid testing technique-shake tables substructure testing", In: *ASCE/SEI Structures Congress and Exposition*, Seattle, WA, USA.

Shao, X., van de Lindt, J., Bahmani, P., Pang, W., Ziaei, E., Symans, M., Tian, J. and Dao, T. (2014), "Real-time hybrid simulation of a multi-story wood shear wall with first-story experimental substructure incorporating a rate-dependent

seismic energy dissipation device", *Smart Struct. Syst., Int. J.*, **14**(6), 1031-1054. https://doi.org/10.12989/sss.2014.14.6.1031
Takanashi, K. and Nakashima, M. (1987), "Japanese activities on on-line testing", *J. Eng. Mech.*, **113**(7), 1014-1032. https://doi.org/10.1061/(ASCE)0733-9399(1987)113:7(1014)
Tu, J.Y. (2013), "Development of numerical-substructure-based and output-based sub structuring controllers", *Struct. Control Health Monitor.*, **20**(6), 918-936. https://doi.org/10.1002/stc.1505
Tu, J.Y., Lin, P.Y., Stoten, D.P. and Li, G. (2010), "Testing of dynamically sub-structured, base-isolated systems using adaptive control techniques", *Earthq. Eng. Struct. Dyn.*, **39**(6), 661-681. https://doi.org/10.1002/eqe.962
Wang, Z., Wu, B., Bursi, O.S., Xu, G. and Ding, Y. (2014), "An effective online delay estimation method based on a simplified physical system model for real-time hybrid simulation", *Smart Struct. Syst., Int. J.*, **14**(6), 1247-1267. https://doi.org/10.12989/sss.2014.14.6.1247
Wang, K.J., Chuang, M.C., Tsai, K.C., Li, C.H., Chin, P.Y. and Chueh, S.Y. (2019), "Hybrid testing with model updating on steel panel damper substructures using a multi-axial testing system", *Earthq. Eng. Struct. Dyn.*, **48**(3), 347-365. https://doi.org/10.1002/eqe.3139
Wang, Z., Xu, G., Li, Q. and Wu, B. (2020), "An adaptive delay compensation method based on a discrete system model for real-time hybrid simulation", *Smart Struct. Syst., Int. J.*, **25**(5), 569-580. https://doi.org/10.12989/sss.2020.25.5.569
Wu, B., Wang, Q., Shing, B.P. and Ou, J. (2007), "Equivalent force control method for generalized real-time substructure testing with implicit integration", *Earthq. Eng. Struct. Dyn.*, **36**(9), 1127-1149. https://doi.org/10.1002/eqe.674
Yang, F., Sedaghati, R. and Esmailzadeh, E. (2021), "Vibration suppression of structures using tuned mass damper technology: A state-of-the-art review", *J. Vib. Control*, **28**(7-8), 812-836. https://doi.org/10.1177/1077546320984305
Yeh, S.W. (2017), "Verification of real-time hybrid tests by shaking table tests for vibration control systems with friction property", Ph.D. Dissertation; National Cheng Kung University, Tainan, Taiwan.
Zhang, Z., Chen, J.B. and Li, J. (2014), "Theoretical study and experimental verification of vibration control of offshore wind turbines by a ball vibration absorber", *Struct. Infrastruct. Eng.*, **10**(8), 1087-1100. https://doi.org/10.1080/15732479.2013.792098
Zhang, Z., Staino, A., Basu, B. and Nielsen, S.R.K (2016), "Performance evaluation of full-scale tuned liquid dampers (TLDs) for vibration control of large wind turbines using real-time hybrid testing", *Eng. Struct.*, **126**, 417-431. https://doi.org/10.1016/j.engstruct.2016.07.008
Zhang, Z., Basu, B. and Nielsen, S.R.K. (2019), "Real-time hybrid aero-elastic simulation of wind turbines with various types of full-scale tuned liquid dampers", *Wind Energy*, **22**(2), 239-256. https://doi.org/10.1002/we.228
Zhao, B., Gao, H., Wang, Z. and Lu, Z. (2018), "Shaking table test on vibration control effects of a monopile offshore wind turbine with a tuned mass damper", *Wind Energy*, **21**(12), 1309-1328. https://doi.org/10.1002/we.2256
Zhou, Z. and Li, N. (2021), "Improving model-based compensation method for real-time hybrid simulation considering error of identified model", *J. Vib. Control*, **27**(21-22), 2523-2535. https://doi.org/10.1177/1077546320961622
Zhu, F., Wang, J.T., Jin, F. and Lu, L.Q. (2017), "Real-time hybrid simulation of full-scale tuned liquid column dampers to control multi-order modal responses of structures", *Eng. Struct.*, **138**, 74-90. https://doi.org/10.1016/j.engstruct.2017.02.004

BS